npj computational materials

www.nature.com/npjcompumats

ARTICLE OPEN

Check for updates

High-throughput design of functional-engineered MXene transistors with low-resistive contacts

Sirsha Guha[1]✉, Arnab Kabiraj[1] and Santanu Mahapatra[1]✉

Two-dimensional material-based transistors are being extensively investigated for CMOS (complementary metal oxide semiconductor) technology extension; nevertheless, downscaling appears to be challenging owing to high metal-semiconductor contact resistance. Here, we propose a functional group-engineered monolayer transistor architecture that takes advantage of MXenes' natural material chemistry to offer low-resistive contacts. We design an automated, high-throughput computational pipeline that first performs hybrid density functional theory-based calculations to find 16 sets of complementary transistor configurations by screening more than 23,000 materials from an MXene database and then conducts self-consistent quantum transport calculations to simulate their current-voltage characteristics for channel lengths ranging from 10 nm to 3 nm. Performance of these devices has been found to meet the requirements of the international roadmap for devices and systems (IRDS) for several benchmark metrics (on current, power dissipation, delay, and subthreshold swing). The proposed balanced-mode, functional-engineered MXene transistors may lead to a realistic solution for the sub-decananometer technology scaling by enabling doping-free intrinsically low contact resistance.

npj Computational Materials (2022)8:202 ; https://doi.org/10.1038/s41524-022-00885-6

INTRODUCTION

In pursuit of the ever-growing need for high-speed integrated circuits with tight power budgets, the exploration of two-dimensional (2D) materials as a replacement for conventional semiconductors has become necessary in the semiconductor industry[1]. The international roadmap for devices and systems (https://irds.ieee.org/) anticipates that the 2D materials will be introduced in the mainstream manufacturing process around 2028. After the first revelation of monolayer molybdenum disulfide (MoS_2) based metal-oxide-field-effect transistors (MOSFET) in 2011[2], integrated circuits built upon 2D transistors have been demonstrated for diverse applications: simple logic inverter[3], 1-bit microprocessor[4], operational amplifier[5], and neuromorphic computation[6]. Meanwhile, various transition-metal dichalcogenides[7–9] and dozens of other 2D materials (e.g., phosphorene[10], tellurene[11], germanane[12], β-TeO_2[13], GeSe[14], etc.) are also investigated as transistor channels. Despite such intense efforts, the high contact resistance at the interface between the 2D material and the external metallic circuits has appeared as the key obstacle for realizing high-performance transistors with sub-decananometer channel lengths. The presence of the Schottky barrier (SB) at this metal–2D interface poses the fundamental challenge in achieving low contact resistance. Approaches like metal work-function engineering, 2D/2D interfacing, graphene/hBN interlayer insertion, and surface charge transfer doping have been attempted to mitigate this effect; however, most of them lack scalability[15]. Unlike a bulk semiconductor, the charge carrier transport in a 2D semiconductor is strongly affected by dopant atoms as the carriers are intrinsically localized to its atomically thin body. Local phase-engineering of MoS_2 crystal[16] is probably the most radical yet scalable solution[17] ever proposed for this problem, which intrinsically eliminates the SB by offering metal-metal contact at the source and drain terminal. Although the concept has recently been extended to borophene crystal[18], finding a stable and synthesizable metallic phase for any 2D semiconductor is highly challenging. The possibility of reverse phase-change due to Joule heating during circuit operation may also be a reliability concern. Complementary (both p and n-type) operation of such phase-engineered devices has also not been demonstrated yet. In passing, we also note that the edge engineering technique may help to tune the work function and to induce metallicity into the MoS_2-H phase[19,20].

Meantime, a new group of non-Van der Waals 2D materials, named MXenes, has gathered tremendous attention since the first report in 2011[21] due to their fascinating mechanical and electronic properties[22–24]. MXenes are transition-metal carbides, nitrides, and carbonitrides with the general formula $M_{n+1}X_nT$, in which a transition metal (M: Ti, Nb, V, Cr, Mo, Ta, etc.) is interleaved with layers of C or N (X), and T indicates surface termination functional groups like OH, = O, and F. Ti_2N, Ti_3C_2, V_4C_3, and Mo_4VC_4 are few examples of MXenes[25,26], which have been synthesized and characterized. MXene possesses a unique electronic property: its bare structure ($M_{n+1}X_n$) is usually metallic; however, with the right functional termination ($M_{n+1}X_nT$), it can become a semiconductor or a metal with a different work function. In this work, we exploit this unique property of MXene to propose an analog of the phase-engineered 2D transistor, which is more versatile than the original. To validate our concept, we develop an automated, high-throughput computational pipeline that performs hybrid density functional theory-based calculations to find 16 complementary (n and p-type) combinations of such transistors by mixing and matching >23,000 materials from an MXene database[27]. It then performs self-consistent quantum transport calculations to simulate their current-voltage characteristics for channel lengths ranging from 10 to 3 nm. The performances of these devices are then assessed against the IRDS requirements, and they are found to meet the benchmark criteria (on current, power dissipation, delay, etc.). The proposed functional-engineered MXene transistor

[1]Nano-Scale Device Research Laboratory, Department of Electronic Systems Engineering, Indian Institute of Science (IISc) Bangalore, Bangalore 560012, India.
✉email: sirshaguha@iisc.ac.in; santanu@iisc.ac.in

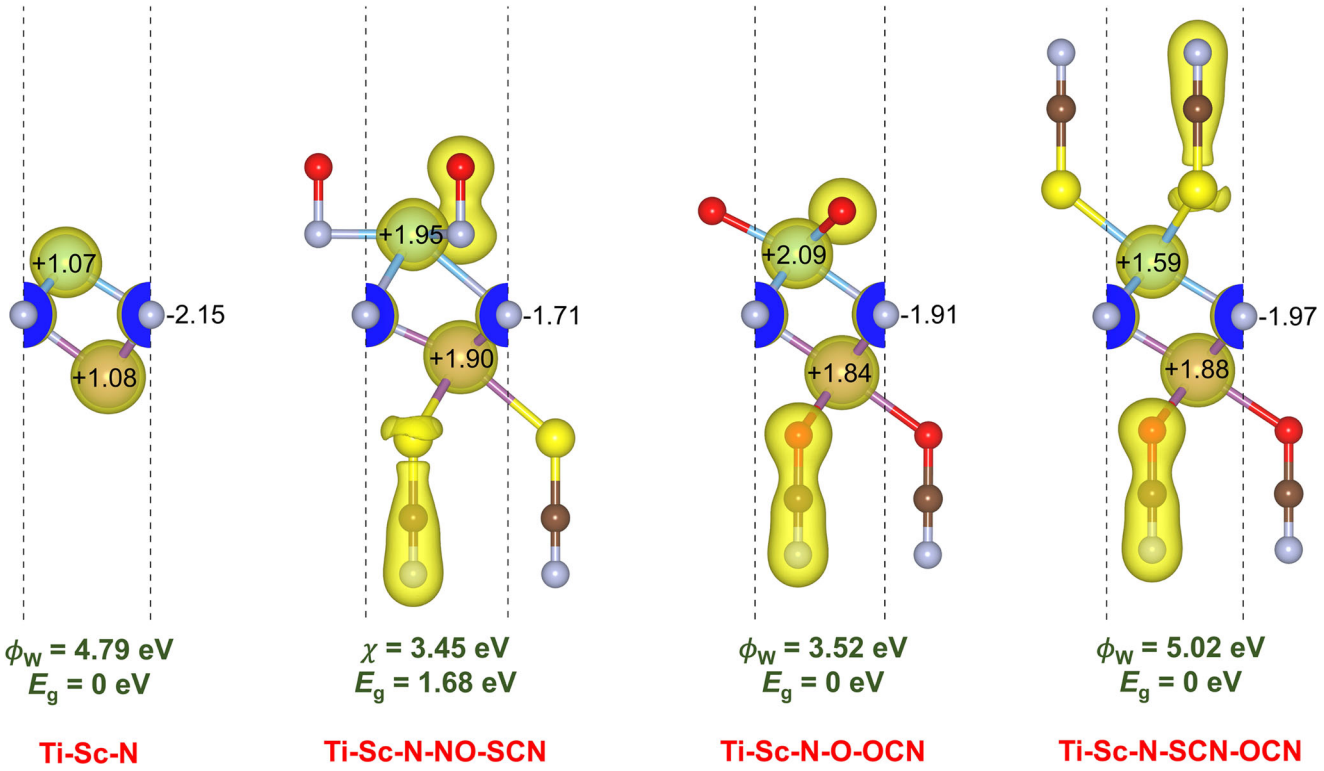

Fig. 1 Variation of work function and band gap of MXene with suitable functionalization. Along with these two quantities, HSE (Heyd–Scuseria–Ernzerhof) hybrid functional-calculated Bader charges for the metal and nitrogen atoms are mentioned for bare metal, functionalized semiconductor, and functionalized metal MXenes with low and high work functions. The yellow and blue clouds represent the HSE-calculated charge densities. The isosurface level is set at 0.17 e Å^{-3}. The dashed lines represent the unit cells. The sky blue, blue, purple, red, brown, and yellow balls represent Ti, N, Sc, O, C, and S atoms.

may lead to a realistic solution for the downscaling of 2D transistors by providing doping-free, intrinsically low-resistive contact and near-balanced-mode complementary operations.

RESULTS

Functionalization of bare MXene

We first allude to how the basic electronic properties, such as band gap and work function, of an MXene, i.e., a material with a fixed bare structure, can be tuned using suitable functional groups. To be consistent with the MXene database, throughout this paper, we are going to identify the single-X ($n = 1$) MXenes in the generalized format M1-M2-X-T1-T2, where M1 and M2 are the metals at the top and bottom, X is C or N, T1 and T2 are the functional groups on the top and bottom side. In Fig. 1, we illustrate the concept of tuning of electronic properties of MXene with suitable functionalization using the example of Ti-Sc-N and its functionalized forms. The bare MXenes are usually metallic and are usually very reactive due to the metal surface terminations[28]. Ti-Sc-N is indeed metallic with an HSE work function $\phi_w = 4.79$ eV. However, when it is functionalized with NO on the top surface and SCN on the bottom surface (i.e., The NO group on the Ti side and the SCN group on the Sc side), the material becomes semiconducting with an HSE band gap of 1.68 eV. The work function also gets modulated to $\phi_w = 4.29$ eV, i.e., the electron affinity becomes $\chi = 3.45$ eV. The HSE-calculated Bader charges and charge density plots reveal a severe, though expected redistribution of charge upon functionalization that reduces negative charge in the N atom and increases positive charge on the metal sites. When Ti-Sc-N is functionalized with O and OCN, we observe a disbalance of charge in the metal atoms compared to Ti-Sc-N and Ti-Sc-N-NO-SCN, i.e., the Ti atom holds significantly more charge than the Sc atom in Ti-Sc-N-O-OCN. The charge in the N site also significantly increases compared to the semiconducting counterpart. This results in a metallic nature in Ti-Sc-N-O-OCN, and the work function significantly reduces to $\phi_w = 3.52$ eV, making this metal suitable for an n-type Schottky contact with the semiconductor with a barrier of $\phi_{Bn} = 0.13$ eV. On the other hand, when Ti-Sc-N is functionalized with SCN and OCN groups, a converse effect is observed. The material becomes metallic again, and the charge at the N site remains at par with that of Ti-Sc-N-O-OCN. However, the charge asymmetry of the metal atoms reverses, i.e., the Sc atom of Ti-Sc-N-SCN-OCN holds significantly more charge than its Ti atom. This results in a significantly high work function of $\phi_w = 5.02$ eV, making this metal suitable for a p-type Schottky contact with the semiconductor with a barrier of $\phi_{Bp} = 0.16$ eV. This example demonstrates how the work function and conductivity of the MXenes can be modulated using strategic functionalization that results in p-type or n-type Schottky contacts among materials with the same bare structure with barrier heights in the desired range.

Functional engineered MOSFET architecture

The basic concept of functional engineered double gate MOSFET architecture is shown in Fig. 2a. In a conventional transistor, channel, source, and drain regions are made up of semiconductors so that it acts as gate-controlled electrical switch. The source and drain regions are heavily doped (n for n-type and p for p-type), while the channel region remains lightly doped or undoped. The high doping in source/drain makes them reservoir of charge carriers, ready to be injected into the channel. High doping also helps to reduce the contact resistance between semiconducting film and the external metallic circuits. In phase-engineered MOSFET, by lithography-assisted chemical treatment, the semiconducting H phase of MoS_2 is converted to the metallic T phase.

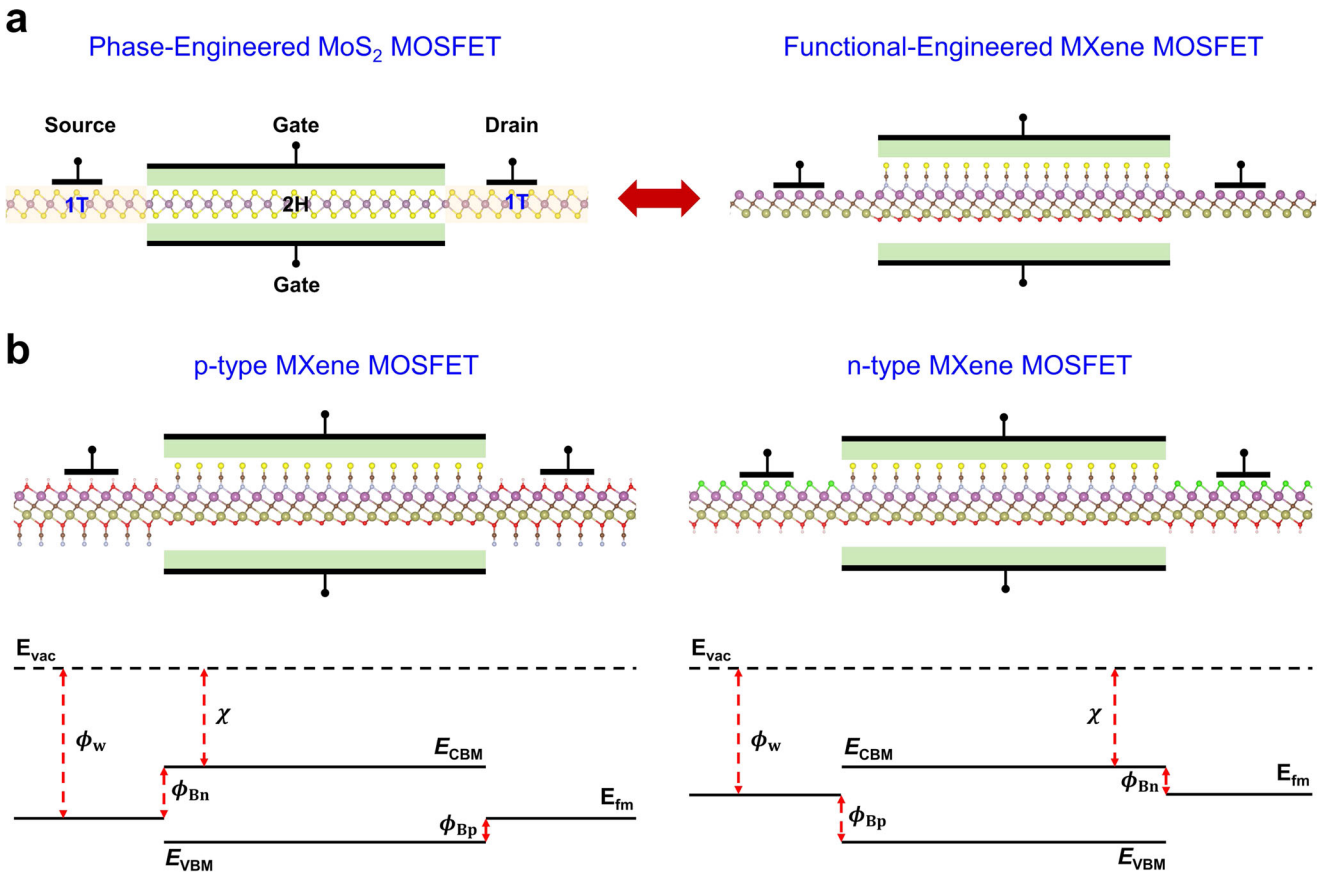

Fig. 2 Concept of functional-engineered MOSFET. a an analogy with phase-engineered MoS_2 transistor **b** complementary p and n-type transistor with source and drain functionalization with their schematic band diagram. Here, E_{vac}, E_{fm}, E_{CBM} and E_{VBM} represent energy levels for vacuum, Fermi, conduction band minima, and valence band maxima, respectively.

Such technique naturally offers a metal-metal, low-resistive interface with outside metal wirings while creating a Schottky junction with the channel interface (instead of a homojunction as happens in the case of a conventional transistor). We propose to implement the same concept with a bare MXene by converting it to a semiconductor in the channel region with strategic functionalization. However, the major drawback of both these approaches is the SB height between source/drain and channel, which is dictated by the work-function difference between the metal-semiconductor (T/H or bare/functionalized) phases and cannot be modulated by the external voltage. Due to the absence of practical, scalable doping technology, these devices either act as p-type or n-type transistors. However, once again, taking advantage of the natural chemistry of MXene, we propose a complementary architecture of MOSFETs, as shown in Fig. 2b. As mentioned earlier, it is possible to tune the work function of bare-MXene with appropriate functionalization while keeping its metallic property intact. For balanced mode complementary operations, a device designer needs to satisfy two conditions: (i) threshold voltages for both p and n-type transistors should be the same (ii) electron and hole mobilities for the channel material need to be equal. In all MXenes studied in this work, we observe light and heavy hole branches in their energy dispersions, and hence it is challenging to satisfy the second criteria. However, the first condition can be met by the appropriate choice of the functional group. Nevertheless, such mixing-matching is a daunting task. In the following section, we discuss how a high-throughput computational pipeline could be designed so that desired complementary combination can be mined from an enormous material space.

High-throughput computational pipeline

A detailed schematic of our high-throughput computational workflow is shown in Fig. 3. In the recent past, the aNANt MXene database (http://anant.mrc.iisc.ac.in/) was introduced, which hosts >23000 2D MXene structures with their PBE (Perdew–Burke-Ernzerhof) level band gaps[27]. The materials hosted here are in the form M1-M2-X-T1-T2, where M1, M2 ϵ {Sc, Ti, V, Cr, Y, Zr, Nb, Mo, Hf, Ta, W}, X ϵ {C, N}, and T1, T2 ϵ {H, O, F, Cl, Br, OH, NO, CN, PO, OBr, OCl, SCN, NCS, OCN}. With recent advances in the synthesis of ordered double transition-metal MXenes[29], the likelihood of realization of the above-mentioned materials has increased significantly. We take the information of the aNANt database as the starting point and screen materials with a PBE bandgap in the range of 0.5–1.0 eV for the semiconducting channel materials. It is well-known that local and semi-local DFT such as PBE severely underestimates a material's band gap compared to experimental findings. On the other hand, hybrid functionals, especially HSE06, have been demonstrated to predict band gaps accurately, albeit being computationally extremely expensive[30]. For our purpose, accurate prediction of electronic properties like band gap and work function is essential as these ultimately decide the Schottky barrier and, in turn, the electrical properties of the potential transistors. From extensive previous experience with PBE and HSE, we chose the above-mentioned specific band gap range in the hope that it would translate to an HSE band gap of 0.8–2.0 eV, the ideal band gap for a transistor channel, in our opinion. Moreover, we only choose MXenes with non-magnetic metal atoms, i.e., M1, M2 ϵ {Sc, Ti, Y, Zr, Hf}. This criterion ensures that the chosen MXenes have an extremely low probability of being magnetic. Determining the magnetic ground state of a material, especially

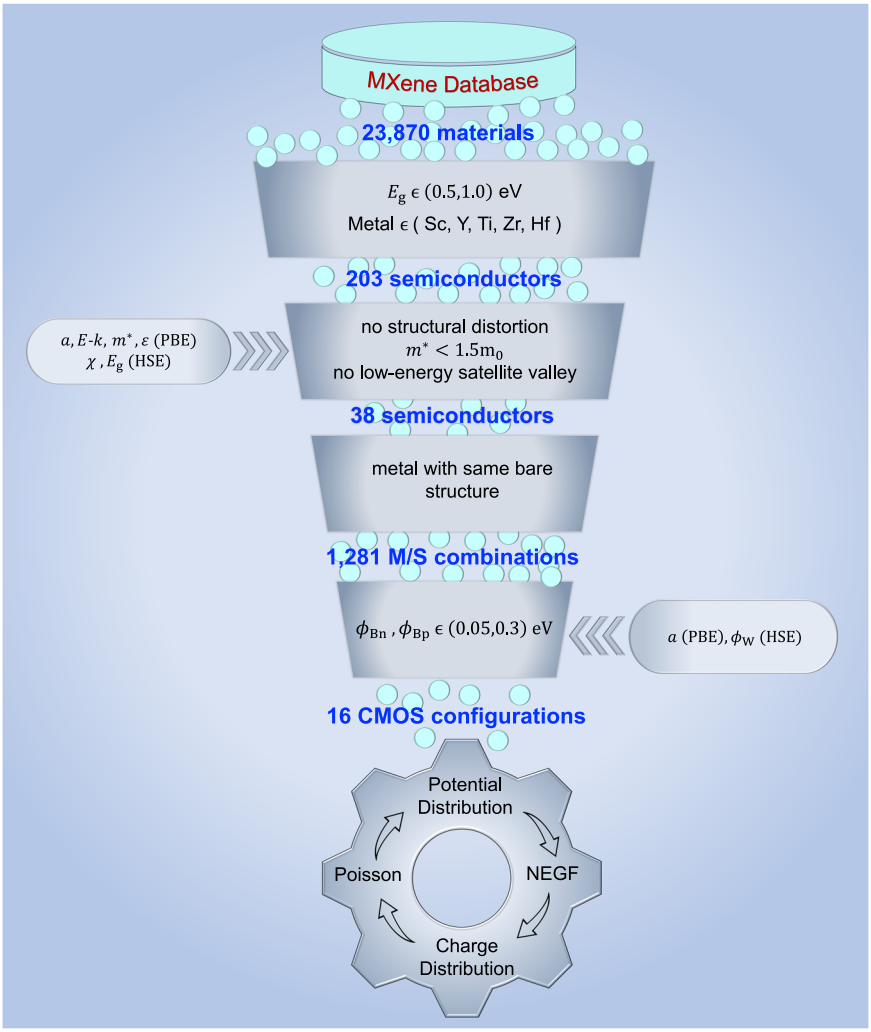

Fig. 3 High-throughput computational pipeline to screen suitable MXene materials for transistor applications and assess their electrical properties.

with two different kinds of magnetic species, can be highly challenging[31], and almost impossible to achieve in a high-throughput study involving thousands of materials. We find 203 semiconductors that satisfy this initial screening criterion.

It appears that most of the structures in the aNANt database might not be optimized[27]. Furthermore, it seems the plane-wave density functional theory (DFT) calculations have been performed without dipole correction, which is essential for accurate electronic property predictions of janus or asymmetric 2D structures. Therefore, we start with PBE structure optimization of the 203 shortlisted semiconductors. After the lattice and ionic relaxation process, the structures are checked for integrity. It was found that several optimized structures, mainly containing the OCl or OBr group, violate the five-level structure of the MXene, and some atom(s) of the functional termination group move between the metal and the X atom. These structures are discarded. To minimize the computational burden (see Methods), we do not include van der Waals (vdW) corrections since its effect is expected to be negligible in monolayer non-vdW materials. We have verified this for two important semiconducting materials (Ti-Sc-N-NO-SCN and Zr-Sc-C-O-OCN) and found the reduction of lattice parameters (0.79% and 0.53%) and change of the ionic positions to be insignificant due to the vdW correction. The crystal structures are provided in Supplementary Data 1.

A PBE-level full band structure is then calculated for the remaining materials. The effective masses are calculated by performing a parabolic fitting of the *E-k* dispersion. Then the materials with an effective mass (m^*) >1.5 m_0 (m_0 is the mass of a free electron) are also discarded since they would result in poor transistor performance. In the cases of anisotropic electron effective masses and heavy and light holes, it was ensured that the lighter electron and the heavy hole effective masses satisfy the above criteria. As discussed later, only the lighter electron effective mass dominates the transport, whereas both hole effective masses remain equally relevant. Judging from the band structure, we also screen out materials with a second local energy minimum/maximum positioned 0.1 eV within the conduction band minimum (CBM)/valence band maximum (VBM) as our quantum transport model relies on low-energy Hamiltonians. After all these screenings, we end up with 38 semiconducting MXenes. A computationally expensive PBE-level linear response-based calculation is performed on these materials to obtain their in-plane static dielectric constant ($\epsilon_{\|}$). A more expensive HSE run is then performed to get the band gaps and work functions of these materials. Note that here we adopt a combined PBE-HSE workflow to strike a reasonable balance between accuracy and computational efficiency. Properties like structural parameters and dielectric functions require extensive calculations, which simply cannot be done at the HSE level for a vast number of materials.

Usually, the PBE prediction is considered accurate enough for these properties[32]. The same can also be said about band curvatures or effective masses. We note that except for the band gap, the PBE and HSE-calculated band structures, including the curvatures at CBM/VBM, are almost identical for MXenes in another widely used database (C2DB)[33,34]. For two materials representing the two different types of band dispersions, we explicitly test out the similarity between the HSE and PBE effective masses and expectedly find these quantities to be very close for most cases. For Ti-Sc-N-NO-SCN, we find, m^*_{ex-PBE}, m^*_{ey-PBE} = (0.90, 0.90) m_0 and m^*_{lh-PBE}, m^*_{hh-PBE} = (0.38, 1.22) m_0, while m^*_{ex-HSE}, m^*_{ey-HSE} = (0.82, 0.82) m_0 and m^*_{lh-PBE}, m^*_{hh-PBE} = (0.35, 1.15) m_0. For Zr-Sc-C-O-OCN, we obtain m^*_{ex-PBE}, m^*_{ey-PBE} = (0.36, 3.45) m_0 and m^*_{lh-PBE}, m^*_{hh-PBE} = (0.34, 0.84) m_0, whereas m^*_{ex-HSE}, m^*_{ey-HSE} = (0.34, 2.52) m_0 and m^*_{lh-PBE}, m^*_{hh-PBE} = (0.31, 0.82) m_0. We note that the prediction error of PBE in the case of m^*_{ey} component of Zr-Sc-C-O-OCN is relatively higher compared to HSE; however, as discussed in the following sections, the m^*_{ex} component, i.e., effective mass in the transport direction dominates the carrier transport in the devices, making this prediction error insignificant.

In the next step, we find all the metallic MXenes from the aNANt database, which share the same bare structure with these 38 semiconductor MXenes. A total of 1281 such metal-semiconductor combinations are identified. All the shortlisted metallic structures are then optimized and checked for structural integrity as described before. After this, the work function of the structurally stable metallic materials and, in turn, the p and n-type Schottky barrier heights when contacted with the corresponding semiconductors are determined using HSE calculations. Only the metals are kept whose contact barrier heights lie in the range ϕ_{Bn}, $\phi_{Bp} \in$ (0.05, 0.3) eV, which is the ideal barrier height for Schottky Barrier Field-Effect Transistors (SBFET). After this step, a total of 16×2 complementary metal-semiconductor combinations are identified, which in addition to satisfying the above criteria, show closely matched p and n-type barrier heights. The calculated important material properties for these 16 semiconductors and 16×2 metals are tabulated in Table 1. It is worth noting that all these 48 metals and semiconductors exhibit negative formation energy ($E_{formation}$) which indicates good thermodynamical stability. Crystal structure information for all these materials in POSCAR format may be found in Supplementary Data 1.

From the band gap and effective mass information of the shortlisted semiconductors, a simple Hamiltonian is then constructed and fed to a self-consistent loop of a Poisson solver and Non-equilibrium Green's Function (NEGF) calculator that calculates the ballistic transport properties of these transistors. From this engine, the electrical characteristics of the SBFETs are obtained, and the results are compared with IRDS specifications. Fine details about the GPU-accelerated high-throughput methodology can be found in the Methods section.

Quantum transport modeling

The essential part of quantum transport modeling is to choose an appropriate Hamiltonian that fits the relevant energy dispersion of the material. The MXene materials inherit a 2D hexagonal first Brillouin Zone (BZ) from their bulk MAX phase, as shown in Fig. 4a. We also observe that the band structure of the 16 shortlisted materials can broadly be categorized into two types, shown in Fig. 4b, c. The VBM is always located at the Γ point with doubly degenerated isotropic light and heavy hole branches for all materials under study. In contrast, the CBM is located either at the Γ or M point with no degeneracy and can exhibit isotropic or anisotropic dispersion. All the semiconducting MXenes show a sizable band gap, and there is no interaction between conduction and valence bands for carrier transport through n- or p-type MOSFETs. Armed with this knowledge, we have chosen separate Hamiltonians for conduction and valence bands that cover all the features of the energy dispersions mentioned above.

For an n-type SBFET, we have chosen a single band effective mass Hamiltonian

$$E(k_x, k_y) = E_{CBM} + \frac{\hbar^2}{2}\left[\frac{k_x^2}{m_{ex}} + \frac{k_y^2}{m_{ey}}\right] \quad (1)$$

where m_{ex} and m_{ey} are effective masses ($m_{ex} \le m_{ey}$) of the electron along the x and y-direction of the device, respectively. We have considered x as the transport direction, which is always aligned to the lower electron effective mass. In contrast, for a p-type SBFET, we have adopted a two-band $k.p$ Hamiltonian[35].

$$H(k_x, k_y) \equiv \begin{bmatrix} \frac{\gamma_1}{2}\left(k_x^2 + k_y^2\right) & \frac{\gamma_2}{2}\left(k_x + ik_y\right)^2 \\ \frac{\gamma_2}{2}\left(k_x - ik_y\right)^2 & \frac{\gamma_1}{2}\left(k_x^2 + k_y^2\right) \end{bmatrix} \quad (2)$$

with $\gamma_1 = \frac{1}{2}\left(\frac{1}{m_L} + \frac{1}{m_H}\right)$ and $\gamma_2 = \frac{1}{2}\left(\frac{1}{m_L} - \frac{1}{m_H}\right)$, where m_L and m_H are light hole and heavy hole effective masses, respectively.

A schematic of the cross-sectional view of the simulated device is shown in Fig. 4d. The Hamiltonians (1) and (2) are first discretized and then fed to the NEGF transport equations, which are solved along with Poisson's equations in a self-consistent loop. The calculations are performed according to the methodology explained in Ref. [35]. However, a Dirichlet boundary condition is enforced at the source/drain-channel junction since we deal with Schottky barrier MOSFET[36]. The value of the Schottky barrier is obtained through DFT calculations as discussed above. We first calculate the electron (or hole) correlation function $G^{n(p)}(k_y, E)$ as:

$$G^{n(p)}(k_y, E) = G(k_y, E)\Sigma_{n(p)}G^{\dagger}(k_y, E) \quad (3)$$

where G (k_y, E) is the retarded Green's function calculated using the discretized Hamiltonian and $\Sigma_{n(p)}$ is obtained from in-scattering self-energies due to source and drain contacts. Next, the carrier density is calculated as,

$$n(p)_q = 2M_v \sum_{k_y} \frac{1}{S}\int_{-\infty}^{+\infty} G^{n(p)}{}_{q,q}(k_y, E)\frac{dE}{2\pi} \quad (4)$$

with $S = L_y \times \Delta x$, where Δx is the discretization step along the direction x and L_y is the length of the device in the direction y. The current density flowing along the x-direction is calculated as,

$$J^{n(p)}{}_{q,q+1} = 2M_v \sum_{k_y} \frac{ie^2}{\hbar L_y}\int_{-\infty}^{+\infty}\left[H_{q,q+1}G^{n(p)}{}_{q+1,q}(k_y, E) - H_{q+1,q}G^{n(p)}{}_{q,q+1}(k_y, E)\right]\frac{dE}{2\pi} \quad (5)$$

The carrier transport is assumed to be ballistic, and spin degeneracy is incorporated by multiplying the whole quantity with a factor of two. In (4) and (5), valley degeneracy (M_v) is equal to 1 for valence band edge and 1 or 3 for conduction band edge, depending on its location in the BZ. The self-consistent NEGF solver has been implemented with GPU acceleration (see Methods), enabling high-throughput transport simulation even in a workstation-grade machine hosting GPUs.

Device simulation and insight into quantum transport

For all the simulations, the parameters are chosen based on the HP (high performance) specifications from the 2020 edition of the International Roadmap for Devices and Systems (IRDS) for the year 2028. To investigate the scaling behavior of the devices, primarily, we have considered the channel length (L_{CH}) to be 10, 7.5, and 5 nm where ballistic transport is predominant. Effective oxide thickness (EOT) and the supply bias (V_{DD}) are set to 0.5 nm and

Table 1. Properties of curated materials.

Bare	Channel	a(Å)	CBM	$E_{formation}$(eV/atom)	E_g, χ(eV)	m^*_{ex}, m^*_{ey}(m_0)	m^*_{lh}, m^*_{hh}(m_0)	$\epsilon_{\|\|}$	Source/Drain	a(Å)	$E_{formation}$(eV/atom)	ϕ_w(eV)	Device Name
Hf-Sc-C	Hf-Sc-C-O-OH	3.28	Γ	−2.20	(0.76, 3.00)	(0.80, 0.80)	(0.26, 0.86)	3.32	Hf-Sc-C-F-H	3.26	−1.79	3.59	M1p
									Hf-Sc-C-NCS-H	3.32	−0.72	3.27	M1n
Sc-Hf-C	Sc-Hf-C-NCS-O	3.33	M	−1.39	(1.68, 3.45)	(0.49, 4.13)	(0.29, 0.81)	3.24	Sc-Hf-C-OH-OCN	3.29	−1.23	5.02	M2p
									Sc-Hf-C-Cl-OH	3.34	−1.89	3.52	M2n
Sc-Hf-C	Sc-Hf-C-SCN-O	3.39	M	−1.18	(1.32, 6.08)	(0.32, 3.49)	(0.24, 0.59)	3.63	Sc-Hf-C-CN-CN	3.35	−0.35	7.23	M3p
									Sc-Hf-C-SCN-Br	3.50	−0.87	6.25	M3n
Sc-Sc-C	Sc-Sc-C-OCl-OCN	3.38	M	−1.09	(1.39, 6.15)	(0.35, 2.19)	(0.43, 1.4)	3.37	Sc-Sc-C-NCO-PO	3.34	−1.18	7.33	M4p
									Sc-Sc-C-O-F	3.25	−2.42	6.38	M4n
Sc-Sc-C	Sc-Sc-C-Br-OCN	3.43	M	−1.14	(1.57, 6.71)	(0.27, 1.47)	(0.36, 1.21)	3.37	Sc-Sc-C-CN-PO	3.37	−0.76	8.11	M5p
									Sc-Sc-C-PO-Cl	3.39	−1.56	6.80	M5n
Sc-Sc-C	Sc-Sc-C-NCO-Br	3.43	M	−1.34	(1.59, 5.12)	(0.26, 1.37)	(0.36, 1.35)	3.42	Sc-Sc-C-NO-NCO	3.32	−0.94	6.55	M6p
									Sc-Sc-C-NO-NCS	3.36	−0.64	5.26	M6n
Sc-Y-C	Sc-Y-C-SCN-Cl	3.64	M	−0.95	(1.24, 6.71)	(0.22, 1.17)	(0.38, 1.25)	3.77	Sc-Y-C-CN-PO	3.49	−0.69	7.84	M7p
									Sc-Y-C-PO-Cl	3.53	−1.52	6.80	M7n
Sc-Zr-C	Sc-Zr-C-SCN-O	3.42	M	−1.15	(1.29, 6.10)	(0.34, 4.41)	(0.25, 0.56)	3.79	Sc-Zr-C-NCO-OCN	3.35	−0.98	7.32	M8p
									Sc-Zr-C-SCN-F	3.43	−1.17	6.17	M8n
Zr-Sc-C	Zr-Sc-C-O-Br	3.39	M	−2.18	(1.77, 4.02)	(0.37, 5.16)	(0.24, 0.65)	3.59	Zr-Sc-C-CN-H	3.33	−0.55	5.55	M9p
									Zr-Sc-C-NO-OH	3.32	−1.29	4.24	M9n
Ti-Hf-C	Ti-Hf-C-O-O	3.16	M	−2.75	(1.46, 4.77)	(0.46, 5.74)	(0.17, 0.31)	4.38	Ti-Hf-C-PO-Br	3.32	−1.65	6.12	M10p
									Ti-Hf-C-O-H	3.14	−1.80	4.83	M10n
Zr-Sc-C	Zr-Sc-C-O-OCN	3.33	M	−1.49	(1.77, 6.44)	(0.36, 3.45)	(0.34, 0.84)	3.22	Zr-Sc-C-CN-SCN	3.48	−0.35	7.92	M11p
									Zr-Sc-C-NO-NCO	3.35	−1.00	6.73	M11n
Y-Zr-C	Y-Zr-C-SCN-O	3.51	M	−1.09	(1.50, 5.93)	(0.41, 5.55)	(0.27, 0.69)	3.68	Y-Zr-C-NCO-OCN	3.46	−0.96	7.34	M12p
									Y-Zr-C-NO-NCO	3.47	−0.93	6.03	M12n
Ti-Sc-N	Ti-Sc-N-NO-SCN	3.43	Γ	−0.87	(1.48, 7.04)	(0.90, 0.90)	(0.38, 1.22)	3.31	Ti-Sc-N-SCN-OCN	3.29	−0.87	8.36	M13p
									Ti-Sc-N-O-OCN	3.13	−1.79	7.17	M13n
Ti-Zr-C	Ti-Zr-C-O-O	3.19	M	−2.67	(1.48, 4.77)	(0.50, 7.00)	(0.18, 0.31)	4.50	Ti-Zr-C-SCN-Br	3.44	−0.98	6.17	M14p
									Ti-Zr-C-NCO-F	3.22	−1.79	4.84	M14n
Zr-Zr-C	Zr-Zr-C-O-O	3.30	M	−2.67	(1.67, 4.21)	(0.32, 2.63)	(0.20, 0.41)	3.58	Zr-Zr-C-CN-Cl	3.39	−1.11	5.73	M15p
									Zr-Zr-C-O-Br	3.37	−2.15	4.34	M15n
Y-Hf-C	Y-Hf-C-SCN-O	3.47	M	−1.12	(1.5, 5.94)	(0.36, 3.87)	(0.26, 0.73)	3.55	Y-Hf-C-NO-SCN	3.54	−0.52	7.30	M16p
									Y-Hf-C-PO-F	3.38	−1.79	6.06	M16n

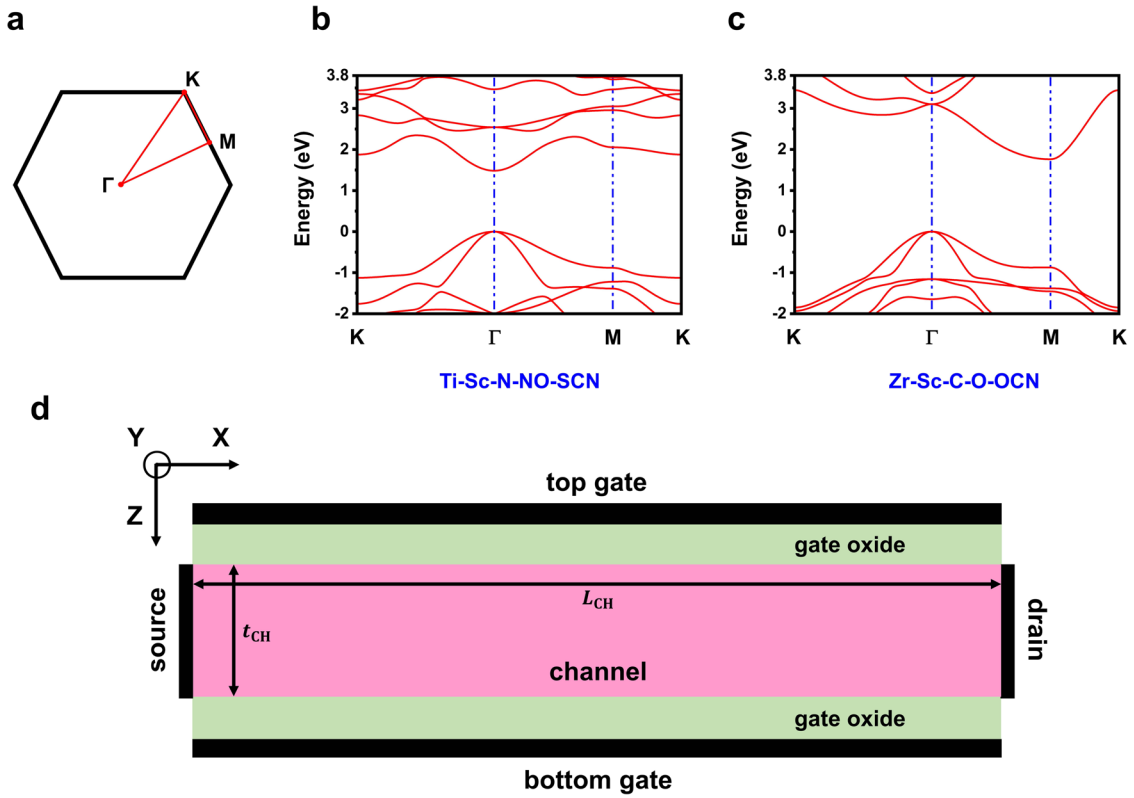

Fig. 4 Electronic properties and device schematic. a 2D hexagonal first Brillouin Zone (BZ) of MXene semiconducting materials. Γ, M, and K are the high symmetry points of the BZ. **b** The HSE band structure of Ti-Sc-N-NO-SCN. VBM and CBM are located at Γ and exhibit isotropic dispersion. **c** The HSE band structure of Zr-Sc-C-O-OCN. VBM is located at Γ and has isotropic dispersion, while CBM is located at M, and the dispersion is anisotropic. **d** Schematic of the cross-sectional (x-z plane) view of the proposed SB transistor.

0.65 V. The thickness of the channel (t_{CH}) is assumed to be equal to the thickness of the monolayer MXene semiconductor (5–9 Å). The gate work function is adjusted so that the OFF-state current (I_{OFF}) at zero gate bias (V_G) becomes 100 nA μm^{-1}.

Transfer characteristics for both n- and p-type devices for each of these 16 MXene semiconductors have been simulated, details of which can be found in Supplementary Data 2. The important figures of merit, such as ON-state current (I_{ON}), Subthreshold swing (SS), intrinsic switching delay time (τ) and power delay product (PDP) are reported in Table 2. I_{ON} is defined as the drain current (I_D) evaluated at $V_G = V_D = V_{DD}$, where V_D represents the drain bias. SS is a key figure of merit, which indicates how fast the transistor can be switched on from the OFF-state with the change of the gate bias. SS has a theoretical minimum value of 60 mV decade^{-1}. For M11 (Zr-Sc-C-O-OCN) and M13 (Ti-Sc-N-NO-SCN), we observe remarkable scalability (minimal degradation of SS till $L_{CH} = 5$ nm) and thus, we have investigated their characteristics further down to $L_{CH} = 3$ nm. Though our investigation is mainly focused for $I_{OFF} = 100$ nA μm^{-1}, we have also calculated ON current for more optimistic OFF current criteria (10 nA μm^{-1}) and presented in Table 2.

To gain insight into the quantum transport process, we have studied the energy-resolved current spectrum superimposed on the band edge profile of device M13 at OFF (Fig. 5b) and ON states (Supplementary Fig. 1). At the ON state, the charge carriers are injected from the source to the conduction/valance band of the channel by quantum mechanical tunneling through a triangular potential barrier. The gate bias controls the drain current by modulating the thickness of this barrier. Supplementary Fig. 1 shows that the current peak occurs at the Fermi level and the tunneling width is a fraction of the channel length. At the OFF state, the thickness of the barrier is too high to enable quantum mechanical tunneling, and carriers are thermionically emitted from the source to the channel over the Schottky barrier. Such over-the-barrier transport limits the subthreshold slope (SS) to 60 mV decade^{-1}. However, as the channel length is scaled-down, a significant component of drain current flows under the barrier, which originates from quantum mechanical tunneling directly from the source to the drain. This under-the-barrier transport component of the OFF current (Supplementary Fig. 2) leads to the degradation of SS and I_{ON} for ultra-short channel devices. From Fig. 5b, we see that the peak of the current spectrum is aligned with the top-of-the barrier for $L_{CH} = 5$ nm, which is then gets split into two for $L_{CH} = 4$ nm. For a 3 nm p-type device, the source-to-drain tunneling is so severe that we see the peak aligned with the Fermi level at the source, far below the top-of-the barrier. The subthreshold and strong inversion regions become somewhat indistinguishable from the $I_D - V_G$ characteristics (Fig. 5a).

An intuitive understanding of all these numerical results could be developed based on the effective masses of the semiconducting channel material. From the basic theory of quantum mechanical tunneling, we know that when an electron/hole tunnels through a barrier, its wave function decays as $\exp(-\beta x)$ within the barrier, where the wave vector β is proportional to the square root of the effective mass of electron/hole. The higher the effective mass, the faster the decay of the wave function. For MXene transistor, the conductivity effective mass m_{ex} is mainly responsible for electron tunneling. However, it is not so straightforward for holes since the bands are degenerate at VBM. When the tunneling width is small (in the case of the ON state), both the light and heavy holes contribute to it and hence the density-of-state effective mass (which is $m_L + m_H$ for 2D systems) should be considered. However, in the case of the OFF state, when the tunneling width is as large as the channel length,

Table 2. Figure of merits of 16 complementary transistors. Triplets are in the order of descending channel length.

Device name	ϕ_B(eV)	I_{OFF} = 100 nA μm^{-1}				I_{OFF} = 10 nA μm^{-1}
		I_{ON}(mA μm^{-1})	τ(fs)	PDP (aJ μm^{-1})	SS (mV decade^{-1})	I_{ON}(mA μm^{-1})
M1p	0.17	(1.42,1.36,1.16)	(32,25,20)	(30,22,15)	(74,75,87)	(1.09,1.05,0.77)
M1n	0.27	(0.64,0.63,0.59)	(34,26,17)	(14,11,7)	(79,80,83)	(0.49,0.48,0.44)
M2p	0.11	(1.42,1.36,1.14)	(35,28,22)	(32,24,16)	(76,77,88)	(1.04,1.01,0.76)
M2n	0.07	(1.56,1.51,1.31)	(34,27,22)	(34,27,19)	(80,81,85)	(1.14,1.10,0.92)
M3p	0.17	(1.51,1.46,1.14)	(30,24,18)	(29,22,13)	(73,75,96)	(1.17,1.09,0.67)
M3n	0.17	(1.93,1.84,1.48)	(27,21,17)	(34,26,17)	(75,76,92)	(1.44,1.36,0.88)
M4p	0.21	(1.097,1.07,0.94)	(43,33,25)	(31,23,15)	(74,75,81)	(0.85,0.81,0.69)
M4n	0.23	(1.78,1.69,1.42)	(27,21,17)	(31,23,16)	(76,78,88)	(1.27,1.26,0.93)
M5p	0.17	(1.21,1.18,1.04)	(41,33,24)	(33,25,16)	(73.7,74,81)	(0.94,0.88,0.73)
M5n	0.09	(2.07,1.98,1.41)	(26,21,18)	(35,27,17)	(74,75,102)	(1.59,1.47,0.71)
M6p	0.16	(1.21,1.17,1.02)	(44,35,26)	(35,26,17)	(70,71,80)	(0.94,0.88,0.7)
M6n	0.14	(2.08,1.98,1.40)	(25,20,18)	(34,26,16)	(73,75,104)	(1.54,1.47,0.68)
M7p	0.11	(1.22,1.17,1.01)	(45,35,26)	(36,27,17)	(70,72,83)	(0.95,0.88,0.74)
M7n	0.09	(2.19,2.07,1.16)	(24,19.4,19)	(34,26,14)	(73,75,127)	(1.62,1.48,0.38)
M8p	0.07	(1.57,1.51,1.17)	(32,25,19)	(32,25,15)	(73,75,97)	(1.22,1.13,0.69)
M8n	0.07	(1.87,1.80,1.46)	(29,23,19)	(36,27,18)	(76,77,89)	(1.39,1.29,0.86)
M9p	0.24	(1.56,1.51,1.27)	(29,23,17)	(30,22,14)	(71,73,89)	(1.16,1.13,0.80)
M9n	0.22	(1.91,1.86,1.62)	(28,22,17)	(34,26,18)	(74,75,83)	(1.42,1.38,1.18)
M10p	0.11	(1.96,1.88,1.11)	(23,18,15)	(29,22,11)	(69,72,134)	(1.51,1.45,0.34)
M10n	0.061	(1.71,1.66,1.46)	(33,26,20)	(37,29,19)	(76,77,83)	(1.27,1.24,1.02)
M11p	0.29	(1.23,1.19,1.08)	(32,25,19)	(26,19,13)	(75,76,82)	(0.92,0.89,0.76)
M11n	0.29	(1.78,1.73,1.50)	(26,21,16)	(31,23,15)	(75,76,84)	(1.33,1.29,1.02)
M12p	0.09	(1.47,1.42,1.16)	(34,27,21)	(33,25,16)	(74,76,90)	(1.14,1.06,0.74)
M12n	0.096	(1.71,1.66,1.41)	(31,25,20)	(35,27,18)	(77,78,85)	(1.28,1.19,0.96)
M13p	0.16	(1.20,1.17,1.03)	(42,33,25)	(33,25,16)	(72,73,80)	(0.97,0.88,0.72)
M13n	0.13	(0.79,0.77,0.71)	(42,32,23)	(22,16,11)	(81,82,86)	(0.59,0.56,0.51)
M14p	0.08	(1.97,1.88,1.15)	(24,18,15)	(30,23,12)	(69,72,127)	(1.52,1.40,0.38)
M14n	0.07	(1.63,1.59,1.39)	(36,29,23)	(38,30,20)	(80,81,84)	(1.22,1.15,0.97)
M15p	0.15	(1.82,1.75,1.28)	(26,21,16)	(31,23,13)	(70,72,107)	(1.40,1.30,0.62)
M15n	0.13	(2.05,1.98,1.66)	(27,22,17)	(36,28,19)	(73,75,86)	(1.58,1.53,1.06)
M16p	0.14	(1.44,1.39,1.14)	(34,27,20)	(32,24,15)	(74,76,90)	(1.08,1.00,0.68)
M16n	0.12	(1.80,1.74,1.45)	(29,23,19)	(35,27,18)	(76,77,86)	(1.34,1.30,0.95)

the wave function of the heavy hole dies within the barrier, and only the light hole is responsible for tunneling. From this understanding, we can say that for a given complementary configuration, the ON current of the p-type device will be higher than that of the n-type if $m_L + m_H < m_{ex}$ and vice versa. For 5 nm or lower channel length devices, this condition might not be applicable if there is significant degradation of SS due to source-to-drain tunneling at the OFF state. Similarly, it can also be said that, for a given complementary configuration, the p-type device will be more susceptible to source-to-drain tunneling if $m_L < m_{ex}$ and vice versa. The numbers in Table 2 follow this simple rule with a soft violation (M10), where the ON currents are almost balanced.

Benchmarking against IRDS

We benchmark the performance of all 2 × 16 devices against the IRDS HP requirements. It can be seen in Fig. 6a that for higher channel lengths I_{ON} is comparable to the IRDS target value (1.979 mA μm^{-1}) at I_{OFF} = 100 nA μm^{-1} for most of the MXene devices. One can correlate the higher I_{ON} with the lower effective masses (m_{ex} for n-type and $m_L + m_H$ for p-type) of the semiconducting channel material. Among all, M15 and M10 are closest to the IRDS target. They also offer near-balanced currents for p and n-type devices. As mentioned earlier, by the appropriate functional-group selection, we can match the barrier heights of the complementary configurations, which leads to almost equal threshold voltages (see Supplementary Fig. 3). However, it is difficult to exactly match the ON currents due to the difference in effective masses. SS is one of the critical figures of merit, which evaluates the gate electrostatic controllability of transistors. It is defined as the change in gate bias required to change the subthreshold drain current by one decade. From Fig. 6b, we can see that for the 10 nm and 7.5 nm channel lengths, many devices exhibit better SS than the IRDS requirements (75 mV decade^{-1}). As discussed before, the leakage current increases for 5 nm channel length, and therefore, the SS and I_{ON} fail to meet the HP requirements, which indicates the degradation of switching behavior of the transistors. The switching speed of transistors is evaluated by intrinsic switching delay time, $\tau = (Q_{ON} - Q_{OFF})/I_{ON}$, where Q_{ON} and Q_{OFF} indicate the overall mobile charge in the device at ON and OFF states, respectively. The power delay product (PDP), defined as PDP $= V_D(Q_{ON} - Q_{OFF})$, represents the energy required to switch the transistor. The calculated τ and PDP are shown in Fig. 6c and d. The τ and PDP gradually decrease as

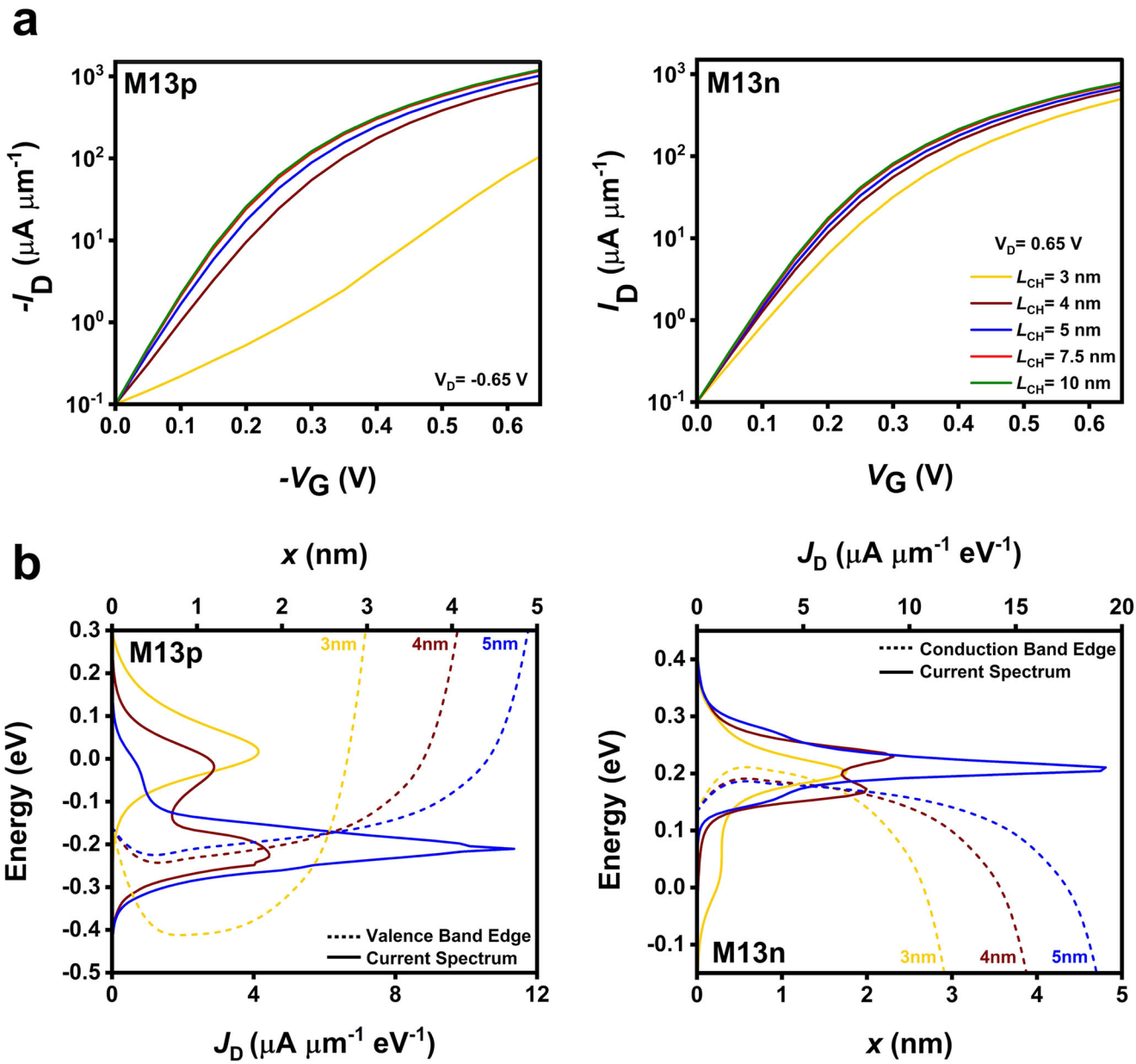

Fig. 5 Device characteristics of M13p and M13n. a Transfer characteristics of transistors at a drain bias of $|V_D| = 0.65$ V for $L_{CH} = 10$ nm to 3 nm. **b** Energy resolved current spectrum (J_D) superimposed on valence (conduction) band edge profile of transistor M13p (M13n) at OFF state for $L_{CH} = 5$ nm to 3 nm.

the channel length shortens. Once again, from Supplementary Fig. 4, we can see that τ and PDP for n- and p-type devices turn out to be nicely balanced for most of the devices.

However, the ON currents for these devices are relatively away from the target with tighter OFF current criteria (10 nA μm^{-1}) as shown in Table 2. While comparing with a recent study[37], we observed that the performance of the proposed functional-engineered MXene transistor is commensurate with most of the 2D materials, while few candidates (P_4, AS_4, etc.) are out-performers due to their lower effective masses (<0.2m_0). However, those materials show inferior performance for 5 nm channel length devices for the same reason. It should be noted that those devices are based on conventional MOSFET architecture with highly doped source-drain regions, whereas our proposed device is doping-free and offers intrinsically low contact resistance.

DISCUSSION

The high-throughput methodology developed in this work to design and assess functional-engineered MXene transistors does have some limitations. For example, the Schottky barrier heights are calculated using the simple Schottky–Mott rule, i.e., $\phi_{Bn} = \phi_w - \chi$, and $\phi_{Bp} = E_g - \phi_{Bn}$. However, it is well known that the barrier height is usually affected by local chemical effects for most real systems[38,39]. In the case of functional-engineered MXene transistor, we expect the interface region to be rather 'seamless,' as the metal and semiconductors both possess the same bare backbone, and therefore chemical changes in the interface region are expected to be minimal. However, functional engineered metal and semiconductor MXenes sharing the same bare structure exhibit a mild to moderate difference in their lattice parameters. The DFT calculated lattice parameters for all relevant metals and semiconductors are given in Table 1. The higher the

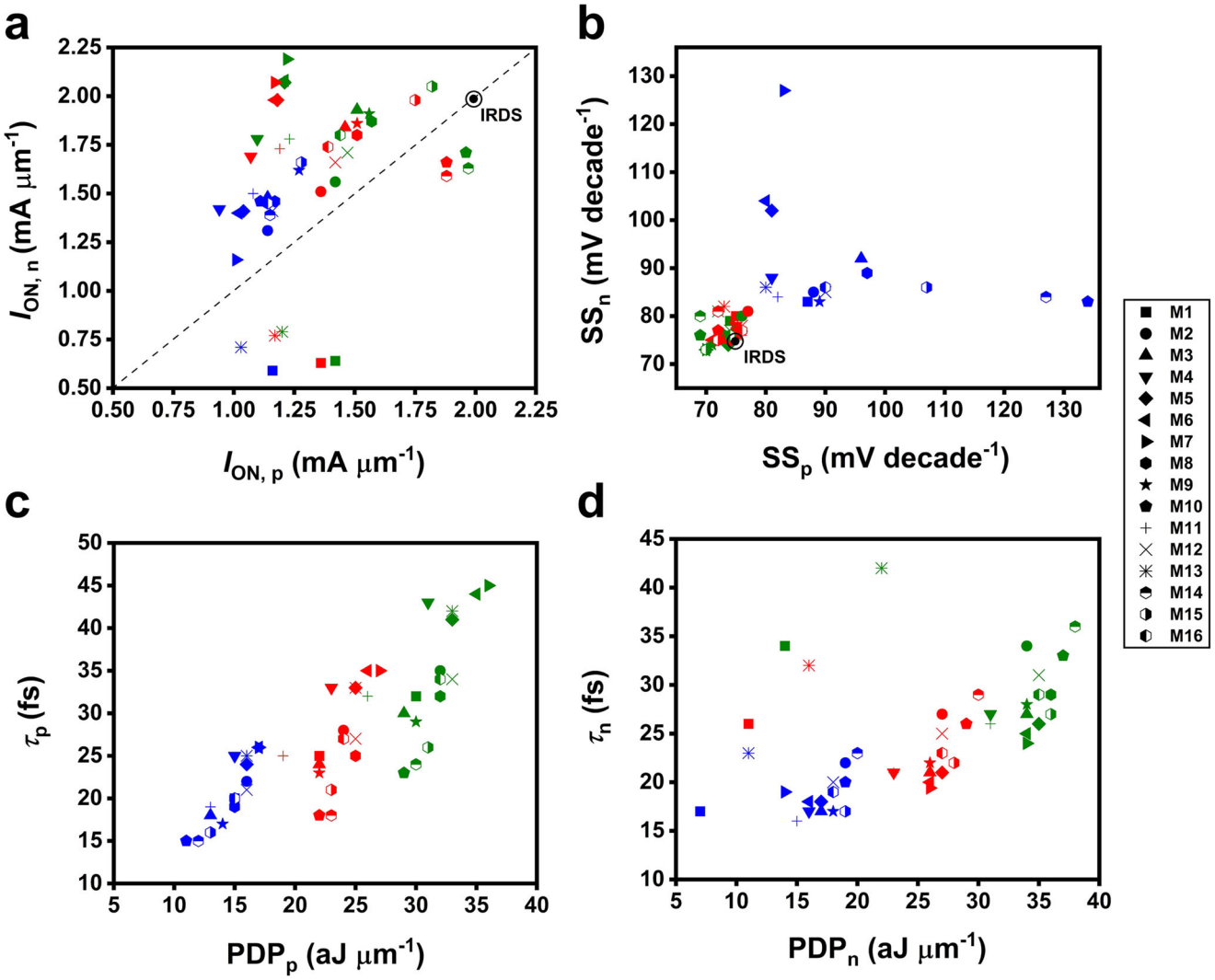

Fig. 6 Performance evaluation of 16 complementary transistors. Performance is evaluated in terms of **a** ON state current I_{ON}. Devices M15, M14, and M10 have I_{ON} close to IRDS predicted value among the 16 devices, **b** subthreshold swing SS. Most of the devices report a value of SS close to the IRDS predicted value, apart from the devices having a channel length of 5 nm. Performance evaluation in the τ-PDP plane of 16 **c** p-type transistors and **d** n-type transistors. Here we use the same color code as Fig. 5.

mismatch between the lattice parameters of the metal and semiconductor, the higher the interfacial strain would be. High interfacial strain might lead to the violation of the Schottky–Mott rule as it can alter the basic material properties such as work function and band gap. Therefore, we expect our predictions to be more reliable in the cases where the lattice mismatch between the metal and semiconductor is mild. Although we have eliminated materials containing magnetic elements through our screening process, heavy elements such as Hf, Ti, and Zr are present in our shortlisted materials. These heavy elements exhibit non-negligible spin-orbital coupling (SOC) effects which may slightly alter the values of material parameters such as bandstructure and work function. This effect is not included in our work since DFT with SOC calculation is computationally highly expensive, especially with the hybrid HSE functional, and unsuitable for a high-throughput study. The effect of SOC may be included in future works for more accurate predictions.

In our transport model, we have adopted simple low-energy parabolic *k.p* Hamiltonian, which immensely helped us to automate the high-throughput computational pipeline. However, it may introduce some inaccuracy since the high-energy energy bands are generally steep, and electrons may have lower effective mass when these are populated. The more rigorous approaches, e.g., DFT-NEGF[40] or MLWF (maximally localized Wannier function)-NEGF[37]-based formalisms capture the entire Brillouin zone and accurately transfer the material chemistry information to the transport model. However, these methodologies are computationally costly, require an extensive computing infrastructure, and usually are not fit for a high-throughput study such as ours. Electron-phonon interaction is another important factor that significantly influences the carrier transport in 2D materials[41–43]. Inclusion of electron-phonon coupling in NEGF formalism not only substantially increases the computational budget but also requires additional DFT-based calculations of deformation potentials. Therefore, this exercise can only be conducted for a few selected devices. Also, our results do not incorporate the effects of parasitic (source/drain contact resistances, interconnect wire capacitances and resistances, etc.), which are evolving with 2D transistor technology. Thus, our estimated figures of merit are optimistically close to the upper limit of the achievable performance. However, using the benchmarking guidelines[44,45] parasitic effects can be included, and even an estimation of performance at the circuit level could be made.

In summary, we propose a doping-free transistor architecture, which exploits an inherent chemical property of MXene to provide intrinsically low-resistive contact at the source and drain terminal. The concept is validated by high-throughput screening of appropriate functional groups and self-consistent quantum transport calculations. Comparison with technology roadmap specifications hints that such a functional-engineered MXene device may provide a technology downscaling solution for 2D transistors. The high-throughput methodology could be extended to multi-metal-layer MXenes, to discover suitable semiconductor-metal combinations for superior performance.

METHODS

DFT setup for high-throughput pipeline

Primary DFT calculations of this work are carried out using the generalized gradient approximation (GGA) as implemented in the code Vienna Ab initio Simulation Package (VASP)[46–49] with the Projector-Augmented-Wave (PAW)[50] method using the PBE[51] exchange-correlation functional. As discussed before, to address the band gap problem[30], the band gaps and work functions of all materials are determined using the hybrid HSE06 functional[52]. The Materials Project recommended pseudopotentials (https://docs.materialsproject.org/methodology/mof-methodology/calculation-parameters/psuedopotentials) have been used throughout. Sufficiently large cutoff energy of 520 eV is used to avoid any Pulay stress. For all structural relaxations, a Gamma-centered *k*-points grid with reciprocal density 150 $Å^{-3}$ is used to sample the Brillouin zone (BZ). A similar *k*-mesh with reciprocal density 750 $Å^{-3}$ is employed for all static runs, including the HSE ones. Electronic convergence is set to be attained when the difference in energy of successive electronic steps becomes $<10^{-6}$ eV, whereas the structural geometry is optimized until the maximum Hellmann–Feynman force on every atom falls below 0.02 eV $Å^{-1}$. A large vacuum space of 25 Å in the vertical direction is applied to avoid any spurious interaction between periodically repeated layers. Dipole correction has been applied for all calculations. The work function of all the materials is calculated as the average of the work function of both sides of the material. This is especially relevant for the cases where the materials possess finite dipole moment, i.e., janus materials[33,34]. All crystal structures are visualized using the tool VESTA[53]. The python libraries pymatgen (Python Materials Genomics) and custodian[54] have been used extensively in the high-throughput pipeline code to achieve full automation. The library Atomic Simulation Environment (ASE)[55] has also been used for some operations. The Sumo toolkit[56] has been used to generate the band structure plots automatically and perform a parabolic fitting of the curvatures of CBM/VBM using five *k*-points to extract the effective masses.

We verified the effect of vdW corrections on the structural parameters of two important semiconductor materials, Ti-Sc-N-NO-SCN and Zr-Sc-C-O-OCN. Various semi-empirical vdW correction schemes, namely the DFT-D3 method of Grimme et al.[57], DFT-D3 with Becke–Johnson (BJ) damping[58], the Tkatchenko–Scheffler method with iterative Hirshfeld partitioning (TS+H)[59–62], and the density-dependent energy correction (dDsC)[63,64], have been tried while performing the structural optimizations. Unfortunately, with the majority of these schemes (DFT-D3, DFT-D3+BJ, and dDsC), we fail to achieve ionic convergence despite trying with all the available VASP built-in optimizers and the optimizers developed by the Henkelman group[65], perhaps because of the MXenes' complex geometry. The TS+H scheme, though costly due to the iterating charge partitioning after every ionic step, is generally well-behaved[66], and we could fully optimize the structures with it.

The elemental reference bulk or molecular structures for calculating the formation energies are taken from the C2DB[33,34], which in turn follows the OQMD for this purpose[67,68].

GPU implementation of transport calculation

The code for NEGF-Poisson calculations has been implemented using Python. In order to incorporate GPU-accelerated computations, the library CuPy[69] has been extensively used. In the case of p-type devices, the carrier and current densities are computed by recursive Green's function algorithm[70], which is a sequential process. We have set L_y to a finite value of 150 nm and primarily, n uniformly spaced transversal wave vectors $k_{y,n} = 2\pi n/L_y$ have been included in the computation to satisfy the Born-von Karman periodic boundary condition in the *y*-direction of the device. As a result, the Hamiltonian and the retarded Green's function are parameterized in terms of k_y and hence, the entire NEGF-Poisson calculation can be computed parallelly for n transversal wave vectors. To achieve this parallelization, the Joblib library (https://github.com/joblib/joblib) is used to write parallel 'for' loops using a multi-processing approach. However, this scheme is not applicable for recursive Green's function algorithm. In a machine comprising an Intel Xeon W-2195, 2.30 GHz processor with 18 cores, 188 GB RAM, and three NVIDIA Quadro RTX 5000 (Turing) 16 GB GPUs, ~1096 s and 3611 s time is required to simulate $I_D - V_G$ characteristic of a 10 nm n- and p-type device, respectively.

DATA AVAILABILITY

The authors declare that the main data supporting the findings of this study are available within the paper and its supplementary files. Other relevant data are available from the corresponding author upon reasonable request.

CODE AVAILABILITY

The details about obtaining VASP, a proprietary code, can be found at https://www.vasp.at/. Other relevant codes are available from the corresponding author upon reasonable request.

Received: 4 May 2022; Accepted: 31 August 2022;
Published online: 21 September 2022

REFERENCES

1. Thomas, S. An industry view on two-dimensional materials in electronics. *Nat. Electron* **4**, 856–857 (2021).
2. Radisavljevic, B., Radenovic, A., Brivio, J., Giacometti, V. & Kis, A. Single-layer MoS2 transistors. *Nat. Nanotechnol.* **6**, 147–150 (2011).
3. Radisavljevic, B., Whitwick, M. B. & Kis, A. Integrated circuits and logic operations based on single-layer MoS2. *ACS Nano* **5**, 9934–9938 (2011).
4. Wachter, S., Polyushkin, D. K., Bethge, O. & Mueller, T. A microprocessor based on a two-dimensional semiconductor. *Nat. Commun.* **8**, 14948 (2017).
5. Polyushkin, D. K. et al. Analogue two-dimensional semiconductor electronics. *Nat. Electron* **3**, 486–491 (2020).
6. Subbulakshmi Radhakrishnan, S., Sebastian, A., Oberoi, A., Das, S. & Das, S. A biomimetic neural encoder for spiking neural network. *Nat. Commun.* **12**, 2143 (2021).
7. Fathipour, S. et al. Exfoliated multilayer MoTe2 field-effect transistors. *Appl Phys. Lett.* **105**, 192101 (2014).
8. Ovchinnikov, D., Allain, A., Huang, Y.-S., Dumcenco, D. & Kis, A. Electrical transport properties of single-layer WS2. *ACS Nano* **8**, 8174–8181 (2014).
9. Jeong, Y. et al. 2D MoSe2 transistor with polymer-brush/channel interface. *Adv. Mater. Interfaces* **5**, 1800812 (2018).
10. Li, L. et al. Black phosphorus field-effect transistors. *Nat. Nanotechnol.* **9**, 372–377 (2014).
11. Wang, Y. et al. Field-effect transistors made from solution-grown two-dimensional tellurene. *Nat. Electron* **1**, 228–236 (2018).
12. Madhushankar, B. N. et al. Electronic properties of germanane field-effect transistors. *2d Mater.* **4**, 21009 (2017).

13. Zavabeti, A. et al. High-mobility p-type semiconducting two-dimensional β-TeO2. *Nat. Electron* **4**, 277–283 (2021).
14. Muhammad, Z. et al. Temperature modulating fermi level pinning in 2D GeSe for high-performance transistor. *Adv. Electron Mater.* **0**, 2101112 (2022).
15. Schulman, D. S., Arnold, A. J. & Das, S. Contact engineering for 2D materials and devices. *Chem. Soc. Rev.* **47**, 3037–3058 (2018).
16. Kappera, R. et al. Phase-engineered low-resistance contacts for ultrathin MoS2 transistors. *Nat. Mater.* **13**, 1128 (2014).
17. Nourbakhsh, A. et al. MoS2 field-effect transistor with Sub-10 nm channel length. *Nano Lett.* **16**, 7798–7806 (2016).
18. Zhang, Y.-L., Yang, J.-H., Xiang, H. & Gong, X.-G. Fully boron-sheet-based field effect transistors from first-principles: inverse design of semiconducting boron sheets. *J. Phys. Chem. Lett.* **12**, 576–584 (2021).
19. Hu, G., Fung, V., Huang, J. & Ganesh, P. Work function engineering of 2D materials: the role of polar edge reconstructions. *J. Phys. Chem. Lett.* **12**, 2320–2326 (2021).
20. Hu, G., Fung, V., Sang, X., Unocic, R. R. & Ganesh, P. Predicting synthesizable multi-functional edge reconstructions in two-dimensional transition metal dichalcogenides. *NPJ Comput Mater.* **6**, 44 (2020).
21. Naguib, M. et al. Two-dimensional nanocrystals produced by exfoliation of Ti3AlC2. *Adv. Mater.* **23**, 4248–4253 (2011).
22. Chaney, G., Çakır, D., Peeters, F. M. & Ataca, C. Stability of adsorption of Mg and Na on sulfur-functionalized MXenes. *Phys. Chem. Chem. Phys.* **23**, 25424–25433 (2021).
23. Anasori, B. et al. Control of electronic properties of 2D carbides (MXenes) by manipulating their transition metal layers. *Nanoscale Horiz.* **1**, 227–234 (2016).
24. Xie, Y. et al. Role of surface structure on Li-ion energy storage capacity of two-dimensional transition-metal carbides. *J. Am. Chem. Soc.* **136**, 6385–6394 (2014).
25. Jiang, X. et al. Two-dimensional MXenes: from morphological to optical, electric, and magnetic properties and applications. *Phys. Rep.* **848**, 1–58 (2020).
26. Deysher, G. et al. Synthesis of Mo4VAlC4 MAX phase and two-dimensional Mo4VC4 MXene with five atomic layers of transition metals. *ACS Nano* **14**, 204–217 (2020).
27. Rajan, A. C. et al. Machine-learning-assisted accurate band gap predictions of functionalized MXene. *Chem. Mater.* **30**, 4031–4038 (2018).
28. Kabiraj, A. & Mahapatra, S. High-throughput assessment of two-dimensional electrode materials for energy storage devices. *Cell Rep. Phys. Sci.* **3**, 100718 (2022).
29. Hong, W., Wyatt, B. C., Nemani, S. K. & Anasori, B. Double transition-metal MXenes: atomistic design of two-dimensional carbides and nitrides. *MRS Bull.* **45**, 850–861 (2020).
30. Borlido, P. et al. Exchange-correlation functionals for band gaps of solids: benchmark, reparametrization and machine learning. *NPJ Comput Mater.* **6**, 96 (2020).
31. Kabiraj, A., Kumar, M. & Mahapatra, S. High-throughput discovery of high Curie point two-dimensional ferromagnetic materials. *NPJ Comput. Mater.* **6**, 35 (2020).
32. Wu, K., Ma, H., Gao, Y., Hu, W. & Yang, J. Highly-efficient heterojunction solar cells based on two-dimensional tellurene and transition metal dichalcogenides. *J. Mater. Chem. A Mater.* **7**, 7430–7436 (2019).
33. Haastrup, S. et al. The Computational 2D Materials Database: high-throughput modeling and discovery of atomically thin crystals. *2d Mater.* **5**, 42002 (2018).
34. Gjerding, M. N. et al. Recent progress of the Computational 2D Materials Database (C2DB). *2d Mater.* **8**, 044002 (2021).
35. Brahma, M., Bescond, M., Logoteta, D., Ghosh, R. K. & Mahapatra, S. Germanane MOSFET for Subdeca nanometer high-performance technology nodes. *IEEE Trans. Electron Devices* **65**, 1198–1204 (2018).
36. Pal, H. S., Low, T. & Lundstrom, M. S. In *2008 IEEE International Electron Devices Meeting* (IEEE, 2008).
37. Klinkert, C. et al. 2-D materials for ultrascaled field-effect transistors: one hundred candidates under the Ab initio microscope. *ACS Nano* **14**, 8605–8615 (2020).
38. Saha, D. & Mahapatra, S. Atomistic modeling of the metallic-to-semiconducting phase boundaries in monolayer MoS2. *Appl Phys. Lett.* **108**, 253106 (2016).
39. Gong, C., Colombo, L., Wallace, R. M. & Cho, K. The unusual mechanism of partial fermi level pinning at metal–MoS2 interfaces. *Nano Lett.* **14**, 1714–1720 (2014).
40. Smidstrup, S. et al. QuantumATK: an integrated platform of electronic and atomic-scale modelling tools. *J. Phys. Condens. Matter* **32**, 015901 (2019).
41. Brahma, M., Kabiraj, A., Bescond, M. & Mahapatra, S. Phonon limited anisotropic quantum transport in phosphorene field effect transistors. *J. Appl Phys.* **126**, 114502 (2019).
42. Cheng, L., Zhang, C. & Liu, Y. Why two-dimensional semiconductors generally have low electron mobility. *Phys. Rev. Lett.* **125**, 177701 (2020).
43. Cao, J. et al. Dissipative transport and phonon scattering suppression via valley engineering in single-layer antimonene and arsenene field-effect transistors. *NPJ 2D Mater. Appl.* **5**, 59 (2021).
44. Nikonov, D. E. & Young, I. A. Benchmarking of beyond-CMOS exploratory devices for logic integrated circuits. *IEEE J. Explor. Solid-State Comput. Devices Circuits* **1**, 3–11 (2015).
45. Pan, C. & Naeemi, A. An expanded benchmarking of beyond-CMOS devices based on Boolean and neuromorphic representative circuits. *IEEE J. Explor. Solid-State Comput. Devices Circuits* **3**, 101–110 (2017).
46. Kresse, G. & Hafner, J. Ab initio molecular dynamics for liquid metals. *Phys. Rev. B* **47**, 558–561 (1993).
47. Kresse, G. & Hafner, J. Ab initio molecular-dynamics simulation of the liquid-metal-amorphous-semiconductor transition in germanium. *Phys. Rev. B* **49**, 14251–14269 (1994).
48. Kresse, G. & Furthmüller, J. Efficient iterative schemes for ab initio total-energy calculations using a plane-wave basis set. *Phys. Rev. B* **54**, 11169–11186 (1996).
49. Kresse, G. & Furthmüller, J. Efficiency of ab-initio total energy calculations for metals and semiconductors using a plane-wave basis set. *Comput Mater. Sci.* **6**, 15–50 (1996).
50. Kresse, G. & Joubert, D. From ultrasoft pseudopotentials to the projector augmented-wave method. *Phys. Rev. B* **59**, 1758–1775 (1999).
51. Perdew, J. P., Burke, K. & Ernzerhof, M. Generalized gradient approximation made simple. *Phys. Rev. Lett.* **77**, 3865–3868 (1996).
52. Heyd, J., Scuseria, G. E. & Ernzerhof, M. Hybrid functionals based on a screened Coulomb potential. *J. Chem. Phys.* **118**, 8207–8215 (2003).
53. Momma, K. & Izumi, F. VESTA3 for three-dimensional visualization of crystal, volumetric and morphology data. *J. Appl Crystallogr* **44**, 1272–1276 (2011).
54. Ong, S. P. et al. Python materials genomics (pymatgen): a robust, open-source python library for materials analysis. *Comput Mater. Sci.* **68**, 314–319 (2013).
55. Hjorth Larsen, A. et al. The atomic simulation environment—a Python library for working with atoms. *J. Phys.: Condens. Matter* **29**, 273002 (2017).
56. Ganose, A. M., Jackson, A. J. & Scanlon, D. O. sumo: Command-line tools for plotting and analysis of periodic *ab initio* calculations. *J. Open Source Softw.* **3**, 717 (2018).
57. Grimme, S., Antony, J., Ehrlich, S. & Krieg, H. A consistent and accurate ab initio parametrization of density functional dispersion correction (DFT-D) for the 94 elements H-Pu. *J. Chem. Phys.* **132**, 154104 (2010).
58. Grimme, S., Ehrlich, S. & Goerigk, L. Effect of the damping function in dispersion corrected density functional theory. *J. Comput Chem.* **32**, 1456–1465 (2011).
59. Tkatchenko, A. & Scheffler, M. Accurate molecular Van Der Waals interactions from ground-state electron density and free-atom reference data. *Phys. Rev. Lett.* **102**, 73005 (2009).
60. Bučko, T., Lebègue, S., Hafner, J. & Ángyán, J. G. Improved density dependent correction for the description of London dispersion forces. *J. Chem. Theory Comput* **9**, 4293–4299 (2013).
61. Bučko, T., Lebègue, S., Ángyán, J. G. & Hafner, J. Extending the applicability of the Tkatchenko–Scheffler dispersion correction via iterative Hirshfeld partitioning. *J. Chem. Phys.* **141**, 034114 (2014).
62. Bultinck, P., van Alsenoy, C., Ayers, P. W. & Carbó-Dorca, R. Critical analysis and extension of the Hirshfeld atoms in molecules. *J. Chem. Phys.* **126**, 144111 (2007).
63. Steinmann, S. N. & Corminboeuf, C. A generalized-gradient approximation exchange hole model for dispersion coefficients. *J. Chem. Phys.* **134**, 044117 (2011).
64. Steinmann, S. N. & Corminboeuf, C. Comprehensive benchmarking of a density-dependent dispersion correction. *J. Chem. Theory Comput* **7**, 3567–3577 (2011).
65. Sheppard, D., Terrell, R. & Henkelman, G. Optimization methods for finding minimum energy paths. *J. Chem. Phys.* **128**, 134106 (2008).
66. Kabiraj, A. & Mahapatra, S. Intercalation-driven reversible switching of 2D Magnetism. *J. Phys. Chem. C.* **124**, 1146–1157 (2020).
67. Saal, J. E., Kirklin, S., Aykol, M., Meredig, B. & Wolverton, C. Materials design and discovery with high-throughput density functional theory: the Open Quantum Materials Database (OQMD). *JOM* **65**, 1501–1509 (2013).
68. Kirklin, S. et al. The Open Quantum Materials Database (OQMD): assessing the accuracy of DFT formation energies. *NPJ Comput Mater.* **1**, 15010 (2015).
69. Okuta, R., Unno, Y., Nishino, D., Hido, S. & Loomis, C. *CuPy: A NumPy-Compatible Library for NVIDIA GPU Calculations*. https://github.com/cupy/cupy (2017).
70. Anantram, M. P., Lundstrom, M. S. & Nikonov, D. E. Modeling of nanoscale devices. *Proc. IEEE* **96**, 1511–1550 (2008).

ACKNOWLEDGEMENTS

The research was funded by the Mathematical Research Impact Centric Support (MATRICS) scheme of the Science and Engineering Research Board (SERB), Government of India, under the grant number MTR/2019/000047. The authors thank Supercomputer Education and Research Centre (SERC), Indian Institute of Science (IISc) Bangalore, for facilitating the Roddam Narasimha cluster (https://www.serc.iisc.ac.in/roddam-narasimha-cluster) for the GPU-based computations. The authors also acknowledge several insightful discussions on quantum transport

with Dr. Biswapriyo Das, Global Foundries Bangalore, and Dr. Madhuchhanda Brahma, the University of Texas at Dallas.

AUTHOR CONTRIBUTIONS

S.G. developed and implemented the Poisson-NEGF code, performed simulations of the devices, and analyzed the transistor characteristics. A.K. developed and implemented the materials exploration part of the high-throughput pipeline and analyzed the materials data. S.M. designed the graphics, conceived the problem statement and overall supervised the work. All authors contributed to writing the manuscript.

COMPETING INTERESTS

The authors declare no competing interests.

ADDITIONAL INFORMATION

Supplementary information The online version contains supplementary material available at https://doi.org/10.1038/s41524-022-00885-6.

Correspondence and requests for materials should be addressed to Sirsha Guha or Santanu Mahapatra.